

# **Distinct element analysis**

## **for Class II behavior of rocks under uniaxial compression**

Hiroyuki SHIMIZU<sup>a\*</sup>, Tomofumi KOYAMA<sup>b</sup>, Tsuyoshi ISHIDA<sup>c</sup>,  
Masakazu CHIJIMATSU<sup>d</sup>, Tomoo FUJITA<sup>e</sup>, Shigeo NAKAMA<sup>e</sup>

- a. Department of Civil and Earth Resources Engineering, Kyoto University  
Kyotodaigaku-katsura, Nishikyo-ku, Kyoto, 615-8540, Japan  
FAX : +81-75-383-3213  
E-mail : Hiroyuki.Shimizu@t01.mbox.media.kyoto-u.ac.jp
- b. Department of Urban and Environmental Engineering, Kyoto University
- c. Department of Civil and Earth Resources Engineering, Kyoto University
- d. Hazama Corporation
- e. Japan Atomic Energy Agency (JAEA)

\*Corresponding author:

Hiroyuki Shimizu, Ph. D student

Department of Civil and Earth Resources Engineering, Kyoto University

Kyotodaigaku-katsura 4, Nishikyo-ku, Kyoto, 615-8540, Japan

FAX: +81-75-383-3213

E-mail: Hiroyuki.Shimizu@t01.mbox.media.kyoto-u.ac.jp

Paper resubmitted to the Int J Rock Mech Min Sci on 25th of June, 2009

## **Abstract**

In this study, the radial strain control method for uniaxial compression tests was introduced in the Distinct Element Method (DEM) codes and the Class II behavior of rocks was simulated. The microscopic parameters used in the DEM models were determined based on laboratory uniaxial compression tests and Brazilian tests carried at Äspö Hard Rock Laboratory, Sweden. The numerical simulation results show good agreement with the complete stress-strain curves for Class II obtained from the laboratory experiments. These results suggest that the DEM can reproduce the Class II behavior of the rock successfully. The mechanism of the Class II behavior was also discussed in detail from the microscopic point of view. The loading condition and microscopic structure of rocks will play an important role for the Class II behavior.

Key words: Uniaxial compression test, Class II behavior, radial strain control, Distinct Element Method (DEM), particle mechanics approaches

## 1. INTRODUCTION

The brittle fracture of rocks is the most studied process in rock mechanics fields and especially the post-peak behavior of rocks is one of the key issues for rock mechanics problems. For the better understanding such a mechanical behavior of brittle rocks, it is fundamental to perform laboratory experiments. In the 1960's, many uniaxial compression tests using high stiff testing machine were carried out to understand the failure mechanism of brittle rocks, and they enable to obtain the post-peak behavior of rocks such as complete stress-strain curves [1, 2]. Wawersik obtained successfully the complete stress-strain curves for various rocks using a stiff testing machine, and classified rock mechanical behavior under uniaxial compression into Class I and Class II according to complete stress-strain curves [3, 4]. As shown in Fig.1, for Class I behavior, axial strain keeps stable even though the axial stress exceeds the peak strength, and the stress-strain curve monotonically increases in axial strain. On the other hand, for the Class II behavior, it suddenly falls into uncontrolled when the axial stress exceeds the peak strength and the curve does not monotonically increase in axial strain. Therefore, it is necessary to control violent collapse of the specimen to obtain the Class II complete stress-strain curve illustrated as the curve OABDE in Fig.1 [5]. Hudson *et al.* conducted the uniaxial compression tests with servo-controlled testing machine in which the radial strain was selected as a control variable, and obtained the Class II complete stress-strain curve successfully [6, 7].



Fig.1

Recently, servo-controlled testing machine is commonly used, and various experimental values were selected as the feedback signal. Sano *et al.* controlled inelastic volumetric strain rate [8]. Terada *et al.* accomplished the servo-controlled uniaxial compression test using AE rate [9]. Okubo *et al.* proposed the control method with linear combination of axial stress and strain [10, 11]. These recently developed servo-controlled testing machines and various testing methods enable to investigate the failure behavior of rock in detail [12, 13]. However, at present, there are still difficulties to obtain complete stress-strain curve of brittle rocks in the laboratory experiments, and the Class II post-peak behavior has not been sufficiently clarified.

Another approach to investigate the failure mechanism and post-peak behavior of rocks is numerical simulation. By rapid advance of computer technology, various numerical analysis techniques have been developed and applied to various problems in the rock engineering fields. Among them, the distinct element method (DEM) [14, 15] with particles can directly represent grain-scale microstructural features of rocks, such as pre-existing flaws, pores, microcracks and grain boundaries. These grain-scale discontinuities in the DEM model induce complex macroscopic behaviors without using complicated constitutive laws/equations. This means that the DEM model may be more

realistic and appropriate representation of rock fracturing comparing with other numerical simulation techniques such as finite element method (FEM) [16-18]. Numerical simulations are strong tool to understand the fracture mechanism and processes of rocks, and some researchers tried to simulate the Class II behavior [19, 20] using different loading control methods. However, it is still difficult to simulate the Class II post-peak behavior by any numerical analysis technique including the DEM, and realistic simulation of the Class II behavior of rock under uniaxial compression has not been achieved actually [21]. Therefore, a new DEM code was developed and Class II behavior of rock was simulated. The objective of this paper is to simulate the uniaxial compression test with radial strain control using a newly developed DEM code, and investigate the Class II post-peak behavior of rocks in detail.

## 2. SIMULATION METHODOLOGY

In this study, two-dimensional distinct element method (2D DEM) was employed. The DEM for granular materials was originally developed by Cundall and Strack [14]. The calculations performed in the DEM can be expressed as the translational and rotational motion of particles with the force and moment acting at each contact of the particles. The force-displacement law is employed to calculate the contact forces and moment generated from the relative motion of particles at each contact. The forces and moment calculated from all contacts on a particle are summed yielding a resultant forces and moment, and Newton's second law gives the translational and rotational motion of particles resulting from the contact force and moment acting between particles. The new state of contacts is re-evaluated by the newly computed translational and rotational motion of particles, and a new cycle of computation is started. Though the DEM is the one of the discontinuum based numerical techniques, it can be applied also to the continuum by introducing bonds between particles [15]. In this section, only a summary of formulation for the mechanical behavior of bonded particles was given. More thorough details of the DEM can be seen in Refs.14 and 15.

### 2.1 Formulation of mechanics of bonded particles

In the two-dimensional DEM, the intact rock is modeled as densely packed small rigid circular particles. Neighboring particles are bonded together at their contact points with three kinds of springs as shown in Fig.2 and interact with each other.

Fig.2

The increments of normal force  $f_n$ , the tangential force  $f_s$ , and the moment  $f_\theta$  can be calculated from the relative motion of the bonded particles, and are given as

$$f_n = k_n (dn_j - dn_i) \quad (1)$$

$$f_s = k_s \left\{ ds_j - ds_i - \frac{L}{2} (d\theta_j + d\theta_i) \right\} \quad (2)$$

$$f_\theta = k_\theta (d\theta_j - d\theta_i) \quad (3)$$

where,  $k_n$ ,  $k_s$  and  $k_\theta$  are the stiffness of normal, shear, and rotational springs, respectively;  $dn$ ,  $ds$  and  $d\theta$  are normal and shear displacements and rotation of particles;  $r_i$  and  $r_j$  are the radii of the bonded particles. A bond between the particles is presented schematically as a gray rectangle in Fig.3, where,  $L$  and  $D$  are the bond length and the bond diameter, respectively.  $D$  is obtained from harmonic mean of the radius of two particles.  $L$  and  $D$  are given by

Fig.3

$$L = r_i + r_j \quad (4)$$

$$D = 2 \cdot \frac{2r_i r_j}{r_i + r_j} \quad (5)$$

Since the DEM is formulated as a fully dynamic system, small amounts of viscous damping are necessary to provide dissipation of high-frequency vibration. If contact damping was not introduced, the assemblies will not be able to reach exact equilibrium condition. Contact damping operates on the relative velocities at the contacts and is represented by dashpots acting in the normal and shear directions at the contact points.

Since the simulation of laboratory rock tests, such as uniaxial compression test, require quasi-static loading, the coefficients of viscous contact damping are determined to provide critical viscous damping that approximates quasi-static loading. The coefficients of viscous contact damping in both normal and shear directions are given by  $C_n$  and  $C_s$ , respectively with the following equations.

$$C_n = 2\sqrt{m_{ij}k_n} \quad (6)$$

$$C_s = C_n\sqrt{k_s/k_n} \quad (7)$$

where,  $m_{ij}$  is given by the weight of two particles  $m_i$  and  $m_j$ .

$$m_{ij} = 2 \frac{m_i m_j}{m_i + m_j} \quad (8)$$

If the stiffness of the springs,  $k_n$ ,  $k_s$  and  $k_\theta$  are set as tuning parameters treated independently, a large effort will be required to determine appropriate values for them. Therefore, the stiffness of the springs,  $k_n$ ,  $k_s$  and  $k_\theta$  are calculated using Timoshenko's beam theory [22], and given by the following equations,

$$k_n = \frac{E_p A}{L} \quad (9)$$

$$k_s = \frac{12E_p I}{(1 + \phi)L^3}, \quad \phi = \frac{12E_p I}{G\kappa AL^2} \quad (10)$$

$$k_\theta = \frac{E_p I}{L} \quad (11)$$

where,  $A$  and  $I$  are the area and moment of inertia of the bonds.  $E_p$  and  $\kappa$  are the Young's modulus of particle and shear correction factors. The shear coefficient  $\kappa$  depends on the shape of the cross-section, and normally,  $\kappa = 5/6$  for a rectangular shape. Shear modulus  $G$  is calculated from Young's modulus  $E_p$  and Poisson's ratio  $\nu_p$ , and given by

$$G = \frac{E_p}{2(1 + \nu_p)} \quad (12)$$

where, young's modulus  $E_p$  and the Poisson's ratio  $\nu_p$  given to the particles are microscopic parameters, and these values are different from Young's modulus and the Poisson's ratio of the rocks obtained from the laboratory experiments and/or simulation of the uniaxial compression tests. The normal stress  $\sigma$  and shear stress  $\tau$  acting on the cross-section of the bond are calculated using the following equations.

$$\sigma = \frac{f_n}{D} \quad (13)$$

$$\tau = \frac{f_s}{D} \quad (14)$$

## 2. 2 Crack generation and classification of crack modes

When  $\sigma$  exceeds the strength of normal spring  $\sigma_c$  or  $\tau$  exceeds the strength of shear spring  $\tau_c$ , then the bond breaks and three springs are removed from the model altogether. Each bond breakage represents generated microcracks.

$$\text{(Bond break criterion 1)} \quad \left. \begin{array}{l} \sigma < 0 \text{ (Tensile stress)} \\ |\sigma| \geq \sigma_c \end{array} \right\} \dots\dots\dots \text{Bond Breakage}$$

$$\text{(Bond break criterion 2)} \quad |\tau| \geq \tau_c \dots\dots\dots \text{Bond Breakage}$$

In the parallel-bond model developed by Potyondy and Cundall [15], the moment acting on the parallel-bond (which is expressed as elastic beam) contributes the normal stress acting on the particles. This means that the bond breakage is judged by the maximum tensile stress acting on the cross section of the assumed elastic beam. On the other hand, in this study, since the spring is introduced to restrict the rotation of the particles and used only to calculate the moment acting on the particles, the normal stress calculated by equation (13) does not include the moment of the elastic beam. This

means that the bond breakage in our model is judged by the average normal stress acting on the cross section of the assumed elastic beam. This is the difference in the mechanism of particle bondage between the parallel-bond model proposed by Potyondy and Cundall [15] and our model presented in this paper.

In the AE measurement during the laboratory experiment, the AE hypocenter can be calculated from the arrival time of the P-wave first motion and the source mechanism of AE events are determined from the spatial distribution of the P-wave first motion polarities. For tensile cracks, all sensors detect the P-wave first motion as compression wave. On the other hand, for shear cracks, both compressional and dilatational P-wave first motions are detected [23]. This polarity of the P wave first motion will depend on the stress state at the crack generation. Therefore, in this study, the crack modes can be classified using shear-tensile stress ratio  $|\tau/\sigma|$  regardless of broken spring type (normal and/or shear springs) as follows.

- |                                    |   |
|------------------------------------|---|
| (Crack classification criterion 1) | $\left. \begin{array}{l} \sigma < 0 \text{ (Tensile stress)} \\  \tau/\sigma  \leq 1 \end{array} \right\} \dots\dots\dots \text{Tensile Crack}$ |
| (Crack classification criterion 2) | $\left. \begin{array}{l} \sigma < 0 \text{ (Tensile stress)} \\  \tau/\sigma  > 1 \end{array} \right\} \dots\dots\dots \text{Shear Crack}$      |
| (Crack classification criterion 3) | $\sigma > 0 \text{ (Compressive stress)} \dots \text{Shear Crack}$  |

When a microcrack is generated, the strain energy stored in both normal and shear springs at the contact point is released. This produces a force imbalance, and subsequent stress redistribution induces an AE event. The magnitude of this AE event is related to the kinetic energy generated in the model which propagates outward from the bond breakage points.

Though the strain energy at the contact point does not directly express the magnitude of AE event, AE generation process mentioned above is induced by the strain energy. For this reason, the strain energy  $E_k$  calculated using equation (15) is assumed to be the energy corresponding to the magnitude of AE event.

$$E_k = \frac{f_n^2}{2k_n} + \frac{f_s^2}{2k_s} \tag{15}$$



### 2.3 Contact behavior between unbonded particles

When the unbonded particles and/or particles with bond breakage are in contact each other, springs and dashpots are introduced into the contact points in both normal and tangential directions, and compressive normal force  $f_n$  and tangential (frictional) force  $f_s$  act at the contact points. The no-tension constraint condition should be satisfied for the springs in the normal direction.

The stiffness of the contact springs in the normal direction is given by the following equation using the compression force  $P$  based on the Hertz's contact theory [24, 25].

$$k_{nn} = \frac{\pi E_p}{2(1-\nu_p^2) \left( \frac{2}{3} + \ln \frac{4r_1}{b} + \ln \frac{4r_2}{b} \right)} \quad (16)$$

$$b^2 = \frac{32(1-\nu_p^2)}{\pi E_p} \cdot \frac{r_1 r_2}{r_1 + r_2} \cdot P \quad (17)$$

where,  $r$  is particle radius and  $b$  is the diameter of the contact surface.  $E_p$  and  $\nu_p$  are Young's modulus and Poisson's ratio of particles, respectively.

When particles and wall boundaries such as loading platen are in contact, the stiffness of contact springs in the normal direction is given by the following equations [24, 25].

$$k_{nn} = \frac{\pi}{\left( \frac{1-\nu_p^2}{E_p} + \frac{1-\nu_w^2}{E_w} \right) \left( \frac{1}{3} + \ln \frac{4r_1}{b} \right)} \quad (18)$$

$$b^2 = \frac{16r_1}{\pi} \left( \frac{1-\nu_p^2}{E_p} + \frac{1-\nu_w^2}{E_w} \right) \cdot P \quad (19)$$

where,  $E_w$  and  $\nu_w$  are Young's modulus and Poisson's ratio of wall.

Equation (16) and (17) represent the contact between cylinders, and Equation (18) and (19) represent the contact between a cylinder and a flat plate. More thorough details of these equations can be seen Refs.24 and 25.

The stiffness of shear contact springs  $k_{ss}$  can be calculated by multiplying the stiffness of the normal contact spring  $k_{nn}$  and stiffness ratio,  $s$  as follows.

$$k_{ss} = s \cdot k_{nn} \quad (20)$$

where stiffness ratio,  $s$  can be calculated from shear modulus  $G$  and Young's modulus  $E$  as

$$s = \frac{G}{E} = \frac{1}{2(1+\nu)} \quad (21)$$

The coefficients of viscous contact damping in both normal and shear directions,  $C_{nn}$  and  $C_{ss}$  can be expressed as,

$$C_{nn} = 2\sqrt{m_{ij} \cdot k_{nn}} \quad (22)$$

$$C_{ss} = C_{nn} \sqrt{k_{ss}/k_{nn}} \quad (23)$$

If the frictional force  $f_s$  exceeds the critical value  $f_{s\max}$ , the slip occurs at the contact points between the particles and frictional force  $f_s$  will be replaced. According to the Coulomb's frictional law, the critical value  $f_{s\max}$  is calculated by the following equation.

$$f_{s\max} = \mu \cdot f_n \quad (24)$$

where  $\mu$  is a coefficient of friction.

As mentioned above, the stiffness of the springs between the bonded particles  $k_n$ ,  $k_s$ ,  $k_\theta$  and unbonded particles  $k_{nn}$ ,  $k_{ss}$  can be calculate from only Young's modulus and the Poisson's ratio using the Timoshenko's beam theory as well as the Hertz's contact theory. As a result, the number of input parameters can be significantly decreased and easily calibrated.

### 3. NUMERICAL SIMULATION FOR VARIOUS ROCK TESTS

#### 3. 1 Experimental data for the simulations

The uniaxial compression tests and Brazilian tests for Äspö diorite were carried out at the Äspö Hard Rock Laboratory (ÄHRL, Sweden) [26]. These experiments were performed using the MTS 815 rock mechanics testing system according to the ISRM (International Society for Rock Mechanics) Suggested Method [27]. Elastic parameters, such as Young's modulus and Poisson's ratio were calculated as secant values between axial stress levels at -0.01% of radial strain and 50% of peak strength. In the uniaxial compression tests, the loading rate was controlled so that the radial strain rate becomes constant. The complete stress-strain curve obtained from the radial strain controlled uniaxial compression tests is presented in Fig.4 and the testing results are summarized in Table.1. As shown in Fig.4, the stress-strain curve obviously shows the Class II behavior. In this study, the radial strain controlled uniaxial tests performed at the ÄHRL were simulated using newly developed DEM code. The input parameters for simulations were carefully calibrated from the laboratory experimental data.

Fig.4

Table.1

#### 3. 2 Radial strain controlled uniaxial compression tests

Fig.5 shows the rock model and the loading condition for the simulation of uniaxial compression tests. The platen under the rock model was fixed and the upper loading platen was moved downward slowly at a certain displacement rate to simulate the uniaxial compression tests. Frictional force was acting between the rock model and the platens. The confining wall was not set along the side of the rock model.

Fig.5

The axial stress applied to the rock model during the compression test was calculated from total force acting on the upper loading platen from particles and model width. The strain is calculated by displacements of the monitored particles. As shown in Fig.5, four particles at the edge of the rock model are selected, and the displacement of these particles was measured. Axial strain  $\varepsilon_1$  and radial strain  $\varepsilon_2$  can be calculated using the following equations.

$$\text{Axial Strain: } \varepsilon_1 = \frac{(y_4^0 - y_2^0) - (y_4^t - y_2^t)}{y_4^0 - y_2^0} \quad (25)$$

$$\text{Radial Strain: } \varepsilon_2 = \frac{(x_3^0 - x_1^0) - (x_3^t - x_1^t)}{x_3^0 - x_1^0} \quad (26)$$

where subscript  $t$  means time.

Young's modulus and Poisson's ratio were calculated as secant values between axial

stress levels at -0.01% of radial strain and 50% of peak strength.

The most common control method for the uniaxial compression test is axial strain control. The axial strain controlled uniaxial compression tests can be easily reproduced in DEM models by moving the upper loading platen downward slowly with constant displacement rate. On the other hands, in the radial strain controlled uniaxial compression tests, loading rate for upper platen should be controlled to keep the radial strain rate constant. Therefore, it is necessary to introduce a special operation for the upper loading platen in DEM models.

As shown in Fig.6, the ideal radial strain rate is manually set firstly, and the error of actual radial strain from ideal value is calculated every loading steps. If the error exceeds the maximum value, the simulation returns to the previous time step, and the simulation is restarted with updated loading rate. This process is repeated until the error becomes within  $\pm 5\%$ , in this study.

Fig.6

Since one particle influences only the adjacent particles in the DEM simulations, some time steps are required to modify the radial strain by changing the loading rate. For this reason, the modification of the loading rate should be done at some time interval. If the modification interval is too small, too many calculation steps are required and as a result, it becomes almost impossible to control radial strain with good accuracy. On the other hand, if the modification interval is too large, it is difficult to control sudden increase and/or decrease of the radial strain. Therefore, the modification of the loading rate is done every 20000 time steps in this study.

### 3. 3 Calibration procedure

For the proper simulations using DEM, appropriate microscopic parameters should be selected [28]. Therefore, preliminary simulations of the uniaxial compression tests, the uniaxial tension tests and the Brazilian tests were performed for the calibration of microscopic parameters, and the microscopic parameters should be adjusted to represent a certain macroscopic mechanical properties. The calibration is usually performed for four tuning parameters, such as young's modulus of the particle, Poisson's ratio, tensile and shear strength for particle bonds. The uniaxial compressive strength (UCS) of the rock model can be obtained from the simulation of the uniaxial compression tests. Moreover, Young's modulus and the Poisson's ratio can be calculated from the stress-strain relations. Since the uniaxial tension tests have been rarely carried out in the laboratory experiments, relatively easy Brazilian tests were generally conducted to obtain the tensile strength of the rock specimen. However, using the DEM, both uniaxial tension test and Brazilian test can be simulated easily. Hence, both the uniaxial tension

test and Brazilian test were performed to calculate accurate tensile strength of the rock models. The calibration process is summarized in Fig.7. Although the actual uniaxial compression tests were performed with radial strain control in Äspö HRL, the DEM model calibration was performed under axial strain control because the radial strain controlled uniaxial compression tests require more computer power and calculation time due to the iterative computation for the modification of the loading rate for the upper platen. For this reason, input microscopic parameters were determined from the axial strain controlled uniaxial compression tests, and the radial strain controlled uniaxial compression tests were simulated using the same microscopic parameters.



Fig.7

## 4. DEM simulations for Class II behavior

### 4. 1 Particle packing procedure

As for the packing process, the particle radius was selected following a uniform distribution between maximum and minimum radius using random number. First, four particles were arranged in the corner of the model as shown in Fig.8(a). Next, particles were aligned along one edge of the model as shown in Fig.8(b) and only the last one particle radius is decided manually to exactly contact with the particle already arranged. This process is repeated four times to enclose the model as shown in Fig.8(c). As shown in Fig.8(d), after arraying particles along the edge of the model, the inside of the model is filled with particles. The new particle was arranged to contact with the pre-existing particles with at least three contact points. This process is repeated until a new particle with minimum radius can not be arranged. When the number of contact points for each particle is less than three, the radius of the particle is modified and/or the position of the particle changed so that the number of contact points become at least three. Using this packing method, it is possible to generate particles in a domain with complicated geometry in relatively short time.

Fig.8

### 4. 2 DEM model for Rock specimen and simulation of laboratory tests

Microscopic properties of the DEM model for rock specimen are summarized in Table.2. As mention above, tuning parameters are determined from calibrations using laboratory testing results (UCS, tensile strength, Young's modulus and Poisson's ratio). The other parameters, such as the shape of the rock model, were the same as the rock specimen used in the laboratory experiments. The size of rock specimen is 5.1cm in width and 14.3cm in height. The number of particles is about 10,000 with the maximum and minimum radius are 0.6mm and 0.3mm, respectively. Young's modulus and the Poisson's ratio values for steel was selected for the wall material properties

Table.2

Koyama *et al.* showed that the variance of the calculated macroscopic mechanical properties such as Young's modulus and Poisson's ratio increase significantly as the number of particles decreases [29]. However, an actual rock specimen contains small grains and minerals. To reproduce such small grains accurately, a great number of particles are necessary. Since the simulation using too many particles requires so long time for calculations and/or sometimes the simulation itself might become impossible, the number of particles and particle radius in this study were selected not only to decrease the variance for calculated values of macroscopic mechanical properties, but also to perform simulations/calculations effectively. For the simulations of the Brazilian tests, a circular shaped rock model was used. Since the number of particles affects

significantly the mechanical properties in DEM, the DEM models of rocks for the Brazilian test was made by the same number of particles and the same distribution of particle radius as the rock model used in the uniaxial compression tests. For this reason, even though the rock specimen used in the actual Brazilian test was 50.9mm in the diameter, the diameter of the rock model for the simulation of Brazilian test was 96mm.

#### 4. 3 Difference of post-peak behavior by load control method

The calibration results are summarized in Table.3. The macroscopic parameters of the rock model show good agreement with the experimental results. The calculated values of mechanical properties obtained from the radial strain controlled uniaxial compression tests were close to the values obtained from the axial strain controlled uniaxial compression tests.

Table.3

The complete stress-strain curve obtained from the simulation with axial strain controlled uniaxial compression tests is shown in Fig.9(a). It is found that the axial strain increase monotonically in the post-peak region, and the stress-strain curve shows clearly the Class I behavior. The complete stress-strain curve obtained from the axial strain controlled uniaxial compression tests can not follow the curve OABDE in Fig.1 because any special axial loading control was not applied. If rock specimens showing Class II behavior are tested with axial strain control, rock specimens will suddenly break as soon as the axial stress exceeds the peak strength and fall into uncontrolled. The complete stress-strain curve will follow the curve OACDE in Fig.1.

Fig.9

On the other hand, Fig.9(b) shows the stress-strain curve obtained from the simulation of the radial strain controlled uniaxial compression tests. As shown in Fig.9(b), the axial strain decreases in the post-peak region to keep the radial strain constant. The complete stress-strain curve shows the Class II behavior and good agreement with the experimental result as shown in Fig.4.

These simulation results show that DEM can reproduce the Class II behavior of brittle rock successfully. Moreover, it was found that only loading control methods affect significantly the post-peak behavior of rocks. It should be noted that the same rock models with same geometry and microscopic input parameters were used for both simulations. This indicates that the loading control methods play important roles for the failure mechanisms and their processes of rocks under uniaxial compression (Class I and II). The microscopic parameter set determined in this section will be named "Case1" later.

## 5. Discussion

### 5. 1 Difference of crack patterns by load control methods

In the previous section, the loading control methods significantly affect on the mechanical behavior of rocks under uniaxial compression. A more detailed discussion will be given in this section mainly focusing on the effects of the loading control methods on the crack generation and propagation, since complex macroscopic behaviors, such as fracture propagation and failure, are strongly controlled by generated microcracks.

Fig.10(a) and (b) show the spatial distribution of microcracks for Case1 with axial and radial strain controlled uniaxial compression tests, respectively. In this figure, tensile and shear cracks are expressed as filled and open circles, respectively. The diameter of the circle corresponds to respective magnitude of AE energy obtained by equation (15). For both control methods, the crack generation pattern in the pre-peak region was similar and most microcracks generated in low stress level were tensile cracks. As the axial stress increases, the number of microcracks increases gradually, and shear cracks starts generating. The detailed discussion on the pre-peak behavior is also seen in Ref. 18.

As shown in Fig.10(a), many shear cracks with relatively large energy were connected along a line in the post-failure region, which is called “shear band”. On the other hand, although a several microcracks were generated and released relatively large energy at the center of the model, shear bands does not appear for the radial strain controlled uniaxial compression tests as shown in Fig.10(b). As shown in Fig.9(a), radial strain increases rapidly when the axial stress exceeds the peak strength for the axial strain controlled uniaxial compression tests. For the radial strain control, on the other hand, to keep the radial strain constant even in the post-peak region, axial loading control was applied and axial load was reduced. As a result, strain energy accumulated in the rock specimen was reduced. Therefore, the cracks released small energy and the formation of the shear band can not grow sufficiently under radial strain control.

Consequently, these simulation results clearly show that the formation of shear bands in the rock specimen plays important roles on post-peak Class I and II behaviors.

Fig.10



## 5. 2 Influence of the rock model properties

In this section, to investigate the effect of microscopic parameters for DEM (the shear and tensile strength of the particles) on the mechanical behavior of rocks under uniaxial compression, especially post-peak Class I and II behaviors, a series of simulations using different values for microscopic parameters were performed.

Among the microscopic parameters, the shear and tensile strength of the particles significantly affect the microcrack generation. Therefore, the different shear-tensile strength ratio was given for each case. The input parameters and calculated material properties of four rock models are listed in Table 4. The microscopic parameters were calibrated using the uniaxial compressive strength and Young's modulus obtained from the laboratory experiments. Noted that the model geometry (particle location and radius) is the same as the one used in Case1.

Table.4

The DEM simulations for uniaxial compression tests with both axial and the radial strain controls were performed, and the complete stress-strain curves were obtained for each case and are shown in Fig.11. As shown in Fig.11, for all cases, the Class I behavior was observed only for the axial strain control, and the Class II behavior was observed in the uniaxial tests with the radial strain control.

Fig.11

Fig.12 shows the microcrack distributions obtained from the axial strain controlled uniaxial compression tests. As shown in Fig.12, microcrack generation was different for each case. When tensile strength is small (Case2), a lot of tensile cracks had been generated in the whole rock specimen. On the other hand, when the tensile strength is large (Case5), the generation of tensile cracks was controlled and fewer tensile cracks were generated. However, clear shear bands appear for all cases when the axial strain controlled method was applied. Similar to Case1 discussed in the section 5.1, these shear bands were not observed when the radial strain controlled method was applied.

Fig.12

From these simulation results, the microscopic parameters (in this case the tensile and shear strength) affect only tensile/uniaxial strength of the rock specimen but do not affect significantly the post-peak Class I and II behaviors. Again the loading conditions (controlled axial and/or radial strain) affect the post-peak behaviors and the formation of shear bands will be key issue.

### 5. 3 Local strain distribution

The DEM simulation results show that the key to understand the Class II behavior is the localized deformation along the shear bands. Hudson *et al.* mentioned in Ref 7 that “. . . as one region of the specimen is loaded and fails, the rest of the specimen remains intact and is elastically loaded and unloaded.” This statement implied that the failure localization and non-uniform failure in rock specimen probably causes the class II behavior. However, the mechanism of non-uniform failure was not sufficiently investigated.

For further discussions, the inside of the rock model was divided into nine local small regions as shown in Fig.13, and local axial strain in each region was measured. The input parameters of Case1 were used for this calculation. The measurement procedure of the local axial strain is similar to the one explained in the section 3.2. Four particles are selected in each region. The radial and axial strain was calculated from the displacement of selected particles using equation (25), (26).

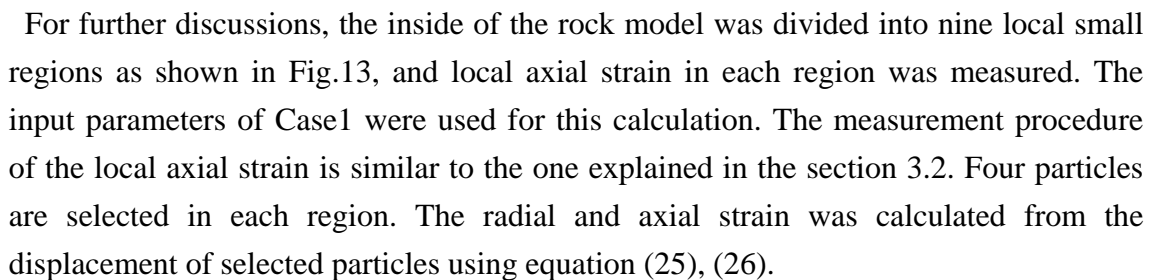


Fig.13

Fig.14(a) shows the relation between a local axial strain for each region and the loading stress obtained from the axial strain controlled uniaxial compression tests. The numbers in Fig.14 represent the region number shown in Fig.13. As shown in Fig.14(a), although the local axial strain recovers in most regions after passing the peak, a significant increase of the axial strain observed in the region No.5. As shown in Fig.10(a), shear bands clearly appear in the axial strain controlled uniaxial compression tests, and the shear bands pass the small region No.5 in Fig.13. This means that an increase of local axial strain in the region No. 5 which was caused by the crack surface slips along the shear bands dominates the mechanical behavior of whole rock specimen and as a result, the complete stress-strain curve shows the Class I behavior.

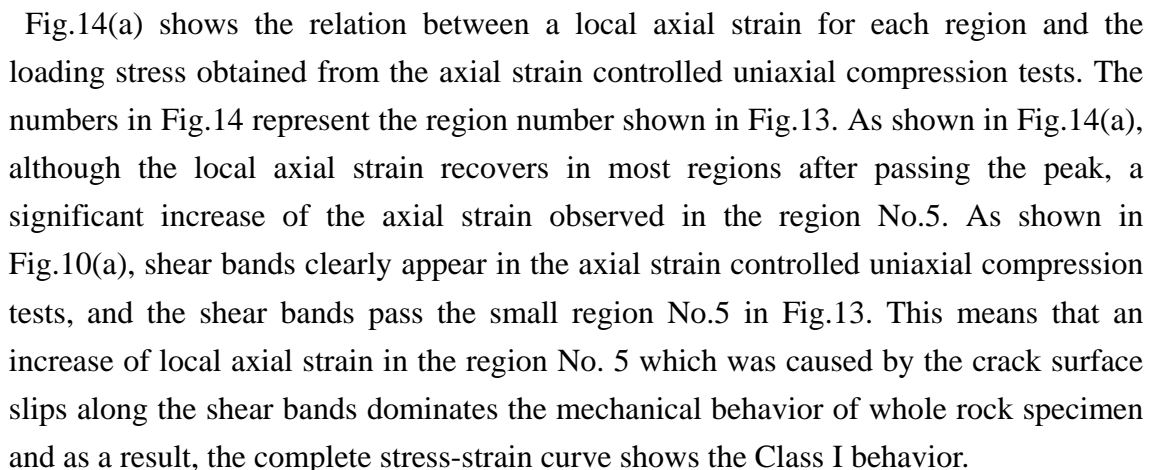


Fig.14

On the other hand, Fig.14(b) shows the relation between a local axial strain in each region and the loading stress obtained from the radial strain controlled uniaxial compression tests. As shown in Fig.14(b), the axial strain recovers in all local small region of rock specimen after the peak stress. This is because the formation of shear band does not grow due to the axial strain control was applied after the peak stress to keep the radial strain constant. Since shear bands were not formed clearly for the radial strain controlled uniaxial compression tests, all local small regions of rock specimen still keep elastic behavior, and as a result, the complete stress-strain curve of rock specimen showed the Class II behavior.

## 6. CONCLUSION

A new DEM code for the uniaxial compression tests with radial strain control was developed and Class II behavior of rock was simulated in this study. The simulation results show good agreement with the complete stress-strain curve obtained from the laboratory experiment. These results suggest that the DEM can reproduce the Class II behavior of the rock successfully. In addition, the mechanism of the Class II behavior was discussed in detail from the microscopic point of view. The findings obtained from this study can be summarized as follows.

1. Although the same rock model and the same input microscopic parameters were used, Class I behavior was obtained in the axial strain controlled uniaxial compression tests and Class II behavior was obtained from the radial strain controlled uniaxial compression tests. This indicates that the loading control methods significantly affect on the mechanical behavior of rocks with uniaxial compression (Class I and II).
2. The pre-peak behavior was almost the same for both loading control methods. However, the mechanical behavior in post-peak region is different between two different loading control methods and the formation of shear bands play important roles in the post-peak region. The shear bands appear clearly in the axial strain controlled uniaxial compression tests. On the other hand, clear shear band does not appear in the radial strain controlled uniaxial compression tests. This is caused by the fact that the formation of shear bands does not grow rapidly due to the axial loading control (unloading) to keep constant radial strain.
3. A series of simulations using different values for microscopic parameters were also carried out and simulation results clearly show that the microscopic parameters do not affect significantly the post-peak Class I and II behaviors. Hence, the key to understand the Class II behavior of brittle rocks is the localized deformation, such as the formation of a shear band.
4. A clear shear bands appear in the axial strain controlled uniaxial compression tests and a significant increase of the axial strain occurs in some small regions of the rock specimen following the crack surface slips along the shear bands. As a result, the stress-strain curve of the entire rocks will show the Class I behavior. On the other hand, since clear shear band is not formed during the radial strain controlled

uniaxial compression tests, most local small regions of rock specimen still keep elastic behavior, and as a result, the complete stress-strain curve of the whole rock specimen shows the Class II behavior.

The post-peak behavior of the rocks was discussed in detail by using newly developed DEM code. The DEM model may be a strong tool to analyze and understand the failure mechanisms and their processes of rocks such as Class II behavior.

Even though the uniaxial compression tests with radial strain control was simulated in this study, many other experimental techniques to obtain the complete stress-strain curves including Class II behavior using various measuring values as the feedback signal to control the loading conditions [8-11]. It is very interesting to simulate and discuss these experimental techniques using DEM. Moreover, it is well-known that the geometry and size of the rock specimen also affect significantly the mechanical behavior in the post-peak region of the rocks [13], which was not investigated in this study. Investigating these issues in detail using DEM will be our future works.

## REFERENCES

- [1] Cook NGW. The failure of rock. *Int J Rock Mech Min Sci*, 1965; 2(4): 389-404.
- [2] Fairhurst CE and Hudson JA. Draft ISRM suggested method for the complete stress-strain curve for intact rock in uniaxial compression. *Int J Rock Mech Min Sci*, 1999; 36: 279-289.
- [3] Wawersik WR. Detailed analysis of rock failure in laboratory compression tests. PhD thesis, University of Minnesota, 1968.
- [4] Wawersik WR and Brace WF. Post-failure behavior of a granite and diabase. *Rock Mechanics*, 1971; 3: 61-85.
- [5] Wawersik WR and Fairhurst C. A Study of brittle rock fracture in laboratory compression experiments. *Int J Rock Mech Min Sci*, 1970; 7(5): 561-575.
- [6] Hudson JA, Brow ET and Fairhurst C. Optimizing the control of rock failure in servo-controlled laboratory test. *Rock Mech*, 1971; 3: 217-224.
- [7] Hudson JA, Crouch SL and Fairhurst C. Soft, stiff and servo-controlled testing machines: A review with reference to rock failure. *Eng Geol*, 1972; 6: 155-189.
- [8] Sano O, Terada M and Ehara S. A Study of the time-dependent microfracturing of oshima granite. *Tectonophysics*, 1982; 84: 343-362.
- [9] Terada M, Yanagidani T and Ehara S. A. E. rate controlled compression test of rocks. In: *Proceedings of the 3rd conference on acoustic emission microseismic activity in geologic structures and materials*. Trans-Tech, Clausthal, 1984; 159-171.
- [10] Okubo S. Uniaxial compression testing using a linear combination of stress and strain as the control variable. *Int J Rock Mech Min Sci*, 1985; 22(5): 323-330.
- [11] Okubo S, Nishimatsu Y and He C. Loading rate dependence of class II rock behaviour in uniaxial and triaxial compression tests—an application of a proposed new control method. *Int J Rock Mech Min Sci Geomech Abstr*, 1990; 27: 559-562.
- [12] Read HE and Hegemier GA. Strain softening of rock, soil and concrete - a review article. *Mech of Materials*, 1984; 3: 271-294.
- [13] Labuz JF and Biolzi L. Class I vs class II stability: A demonstration of size effect. *Int J Rock Mech Min Sci*, 1991; 28: 199-205.
- [14] Cundall PA and Strack ODL. A discrete numerical model for granular assemblies. *Geotechnique*, 1979; 29(1): 47-65.
- [15] Potyondy DO and Cundall PA. A bonded- particle model for rock. *Int J Rock Mech Min Sci*, 2004; 41: 1329-1364.
- [16] Potyondy DO. Simulating stress corrosion with a bonded-particle model for rock. *Int J Rock Mech Min Sci*, 2007; 44: 677-691.

- [17] Shimizu H, Murata S and Ishida T. The applicability of distinct element modeling for rock fracture. *Journal of MMIJ*, 2008; 124(12): 777-784. (in Japanese)
- [18] Shimizu H, Murata S and Ishida T. Distinct element analysis for rock failure under uniaxial compression. *Journal of MMIJ*, 2008; 125(3): 91-97. (in Japanese)
- [19] He C, Okubo S and Nishimatsu Y. A study on the Class II behavior of rock. *Rock Mech and Rock Eng*, 1990; 23: 261-273.
- [20] Pan P-Z, Feng X-T and Hudson JA. Numerical simulations of Class I and Class II uniaxial compression curves using an elasto-plastic cellular automaton and a linear combination of stress and strain as the control method. *Int J Rock Mech Min Sci*, 2006; 43(7): 1109-1117.
- [21] Bäckström A, Antikainen J, Backers T, Feng X-T, Jing L, Kobayashi A, Koyama T, Pan P-Z, Rinne M, Shen B and Hudson JA. Numerical modelling of uniaxial compressive failure of granite with and without saline porewater. *Int J Rock Mech Min Sci*, 2008; 45(7): 1126-1142.
- [22] Timoshenko SP and Goodier JN. *Theory of Elasticity* 2nd edition. McGraw-Hill Book Company, 1951.
- [23] Kasahara K. *Earthquake mechanics*. Cambridge university press, 1981; 38-42.
- [24] Roark RJ and Young WC. *Formulas for Stress and Strain* 5th Edition. McGraw-Hill Book Company, 1975.
- [25] Landau LD and Lifshitz EM. *Theory of Elasticity*. Pergamon Press, Oxford, 1986.
- [26] Staub I, Andersson JC and Magnor B. Äspö Pillar Stability Experiment, geology and mechanical properties of the rock mass in TASQ. SKB report R-04-01, Stockholm, 2004; 81-84.
- [27] Brown ET. *Rock characterization, testing and monitoring: ISRM. suggested methods*. Pergamon Press, 1981; 210.
- [28] Yoon J. Application of experimental design and optimization to PFC model calibration in uniaxial compression simulation. *Int J Rock Mech Min Sci*, 2007; 44(6): 871-889.
- [29] Koyama T and Jing L. Effects of model scale and particle size on micro-mechanical properties and failure processes of rocks - A particle mechanics approach. *Engineering Analysis with Boundary Elements*, 2007; 31(5): 458-472.

## **CAPTIONS for TABLES**

Table1 Laboratory tests and testing results.

Table2 Rock model properties.

Table3 Calibration results.

Table4 Four data sets with different values for microscopic parameters.

## **CAPTIONS for FIGURES**

Fig.1 Representative figures for stress-strain curves of class I and class II behavior of rock failure under uniaxial compression.

Fig.2 Three kinds of springs between two bonded particles.

(a) Normal spring.

(b) Shear spring.

(c) Rotational spring.

Fig.3 Bonded particles model.

Fig.4 Complete stress-strain curve obtained by using the radial strain controlled loading method <sup>26</sup>.

Fig.5 Loading condition for the simulation of uniaxial compression tests. The measuring points for the axial and radial strain were located slightly inside from the edge of the rock model. The distance between two measuring points is 90% of the rock model width or height.

Fig.6 Simulation procedure for radial strain controlled uniaxial compression test.

Fig.7 Calibration process.

Fig.8 Particle packing method.

- (a) Four particles are arranged in the corner of the model.
- (b) Particles are aligned along one side of the model.
- (c) Process (b) is repeated four times to enclose the model.
- (d) Put on a new particle tangent to the pre-existing particles.

Fig.9 Complete stress-strain curves obtained from the simulation with different controlling methods.

- (a) Axial strain control.
- (b) Radial strain control.

Fig.10 Spatial distribution of all the cracks for case1 in pre-failure region (left) and post-failure region (right). (a) axial strain control and (b) radial strain control. Tensile and shear cracks are expressed as filled and open circles, respectively. The diameters of each circle correspond to their respective magnitudes of energy.

- (a) Axial strain control.
- (b) Radial strain control.

Fig.11 Complete stress-strain curves obtained from each case.

- (a) Axial strain control.
- (b) Radial strain control.

Fig.12 Spatial distribution of all the cracks for each cases. These figures are obtained from axial strain controlled uniaxial compression tests. Tensile and shear cracks are expressed as filled and open circles, respectively. The diameters of the circles correspond to their respective magnitudes of energy.

Fig.13 Local strain monitoring procedure in each region.

Fig.14 Local stress-strain curves in each region. The numbers in the figure represent the region number shown in Fig.13.

- (a) Axial strain control.
- (b) Radial strain control.



Table1 Laboratory tests and testing results.

<b>TEST DATA</b>			
Client:	SKB	Loading Control:	Radial Strain Rate
Test:	Uniaxial	Equivalent Loading Rate:	0.75 MPa/s
Equipment:	MTS 815	Confining Stress:	0 MPa
Test Date:	2003-06-10		
<b>SPECIMEN DATA</b>			
Site:	Äspö	Diameter:	50.9 mm
Type:	Diorite	Length/Diameter:	2.80
Hole:	KA3376B01	Density:	2742 kg/m <sup>3</sup>
Depth:	33.32 m		
<b>TEST RESULTS</b>			
Peak Strength:	195.1 MPa	Young's Modulus:	67.4 GPa
Tensile Strength:	15.5 MPa	Poisson's Ratio:	0.27

Table2 Rock model properties.

<b>ROCK MODEL DATA</b>	
Rock model for simulation of uniaxial compression (tension) test	
Width:	51mm
Height:	143mm
Number of particles:	9457
Rock model for simulation of Brazilian test	
Diameter:	96mm
Number of particles:	9401
Maximum particle radius:	0.6mm
Minimum particle radius:	0.3mm
Particle density:	2742 kg/m <sup>3</sup>
Friction coefficient of particle:	0.5
Friction coefficient of wall:	0.3
Young's modulus of wall ( $E_w$ ):	200GPa
Poisson's Ratio of wall ( $\nu_w$ ):	0.3
<b>TUNING PARAMETERS</b>	
Young's modulus of particle ( $E_p$ ):	146.0 (GPa)
Poisson's Ratio of particle ( $\nu_p$ ):	0.2
Shear strength of bonding ( $\tau_c$ ):	245.0 (MPa)
Tensile strength of bonding ( $\sigma_c$ ):	60.0 (MPa)

Table3 Calibration results.

	Experiment	Simulation	
	Radial	Axial	Radial
Loading control:			
UCS of rock model (MPa):	195.10	195.47	200.65
Young's modulus of rock model (GPa):	67.40	67.63	67.55
Poisson's Ratio of rock model:	0.270	0.276	0.286
Tensile strength of rock model (MPa)			
Brazilian test:	15.50		15.51
Uniaxial tension test:	-		16.05

Table4 Four data sets with different values for microscopic parameters.

<b>-Input parameters-</b>	<b>Case2</b>	<b>Case3</b>	<b>Case4</b>	<b>Case5</b>
Shear strength of bonding ( $\sigma_c$ MPa):	320	255	198.5	162.5
Tensile strength of bonding ( $\tau_c$ MPa):	32	51	99.25	162.5
Shear/Tensile strength ratio	10	5	2	1
Young's modulus of particle ( $E_p$ GPa):	170.0	150.0	140.0	142.0
Poisson's Ratio of particle ( $\nu_p$ ):	0.2	0.2	0.2	0.2
<b>-Results (Axial strain control)-</b>				
UCS of rock model (MPa):	195.93	196.08	194.97	194.66
Young's modulus of rock model (GPa):	67.83	67.52	67.06	67.96
Tensile strength of rock model (MPa):	8.59	13.69	26.56	43.50

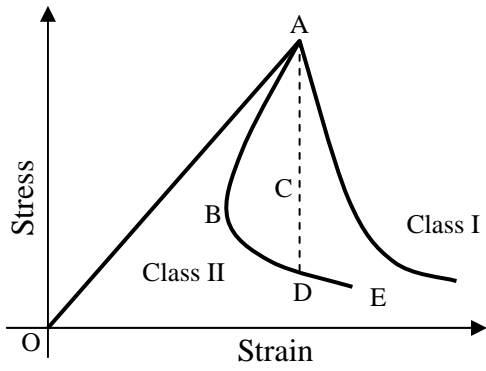


Fig.1 Representative figures for stress-strain curves of class I and class II behavior of rock failure under uniaxial compression.

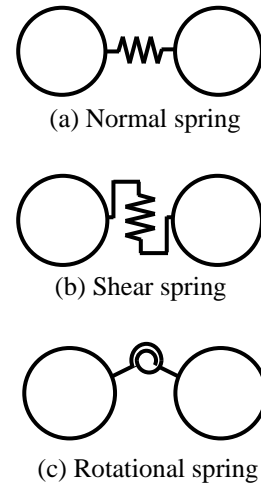


Fig.2 Three kinds of springs between two bonded particles.

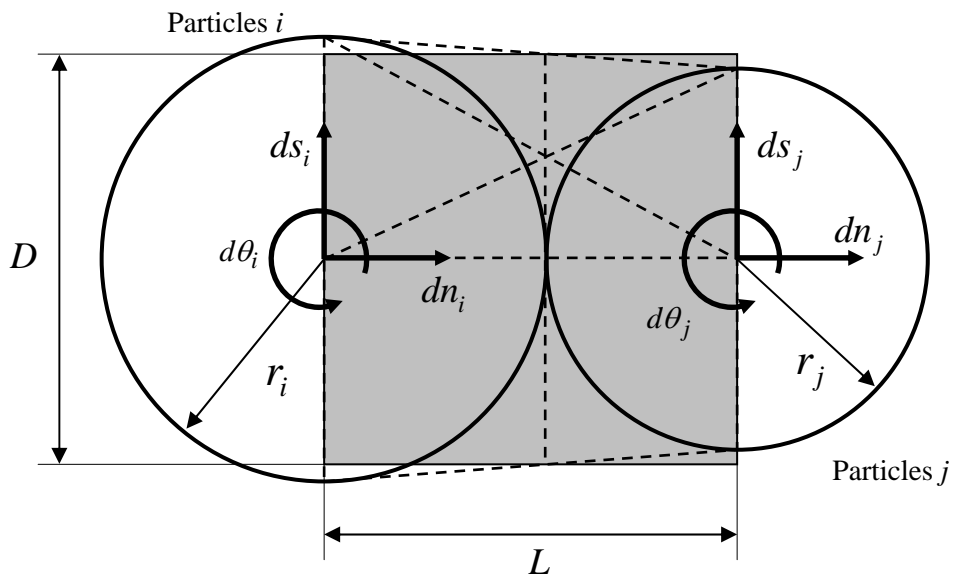


Fig.3 Bonds particles model.

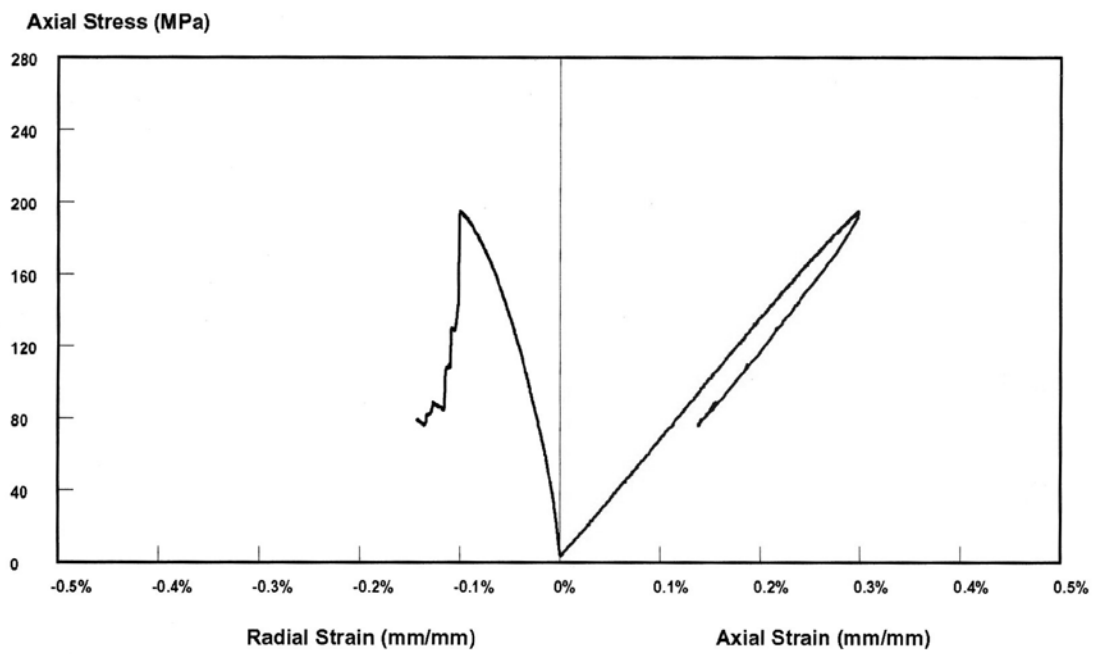


Fig.4 Complete stress-strain curve obtained by using the radial strain controlled loading method <sup>26)</sup>.

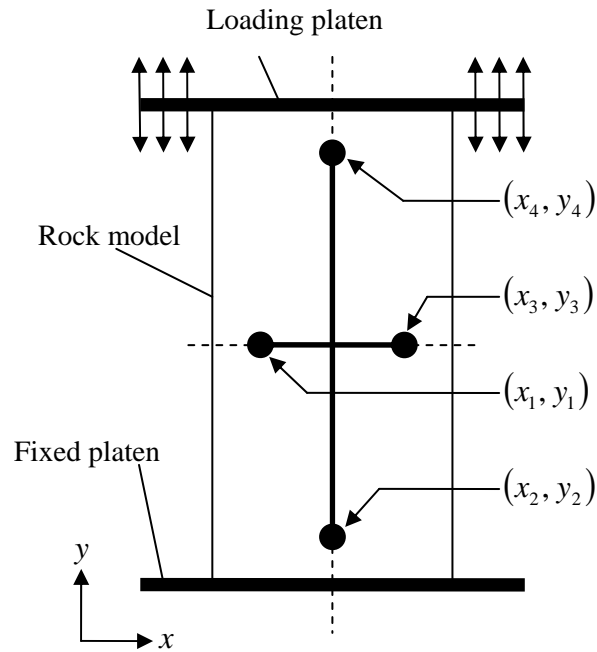


Fig.5 Loading condition for the simulation of uniaxial compression tests. The measuring points for the axial and radial strain were located slightly inside from the edge of the rock model. The distance between two measuring points is 90% of the rock model width or height.

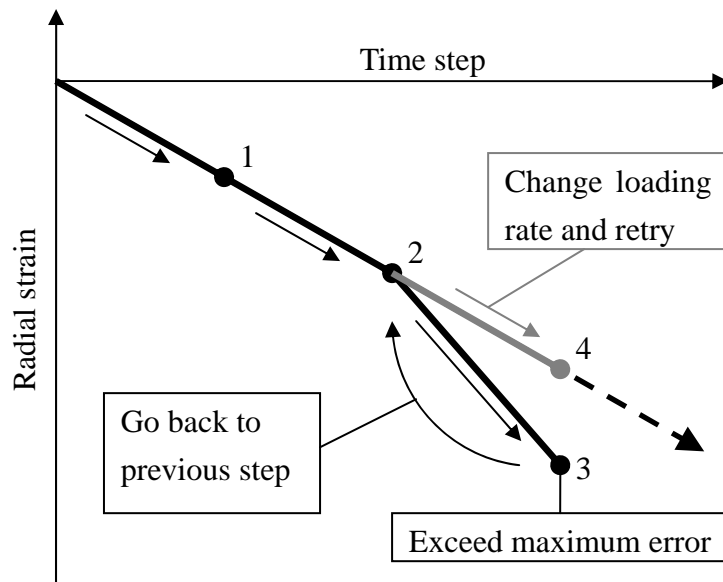


Fig.6 Simulation procedure for radial strain controlled uniaxial compression test.

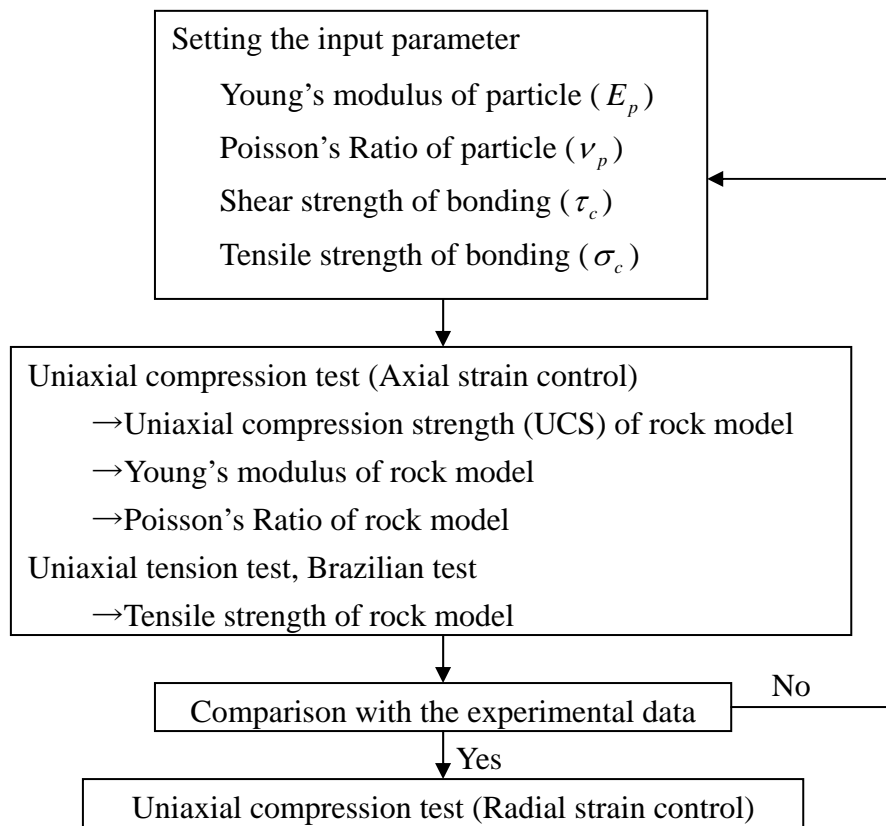
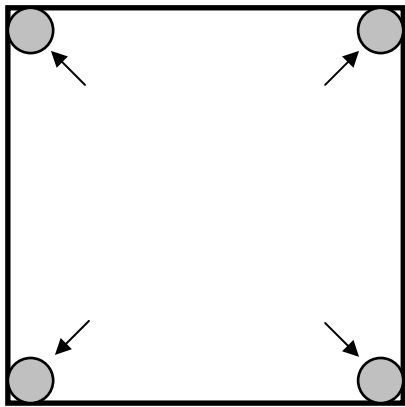
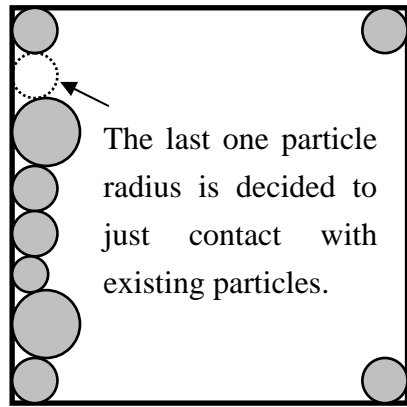


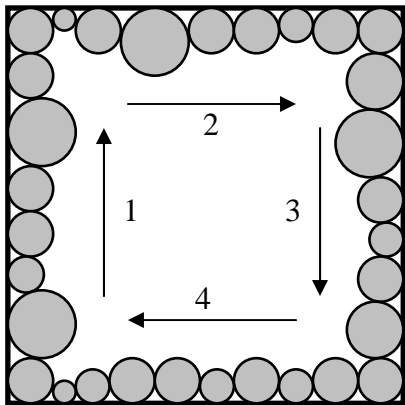
Fig.7 Calibration process.



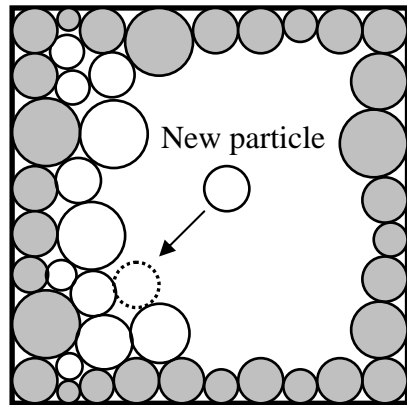
(a) Four particles are arranged in the corner of the model.



(b) Particles are aligned along one side of the model.



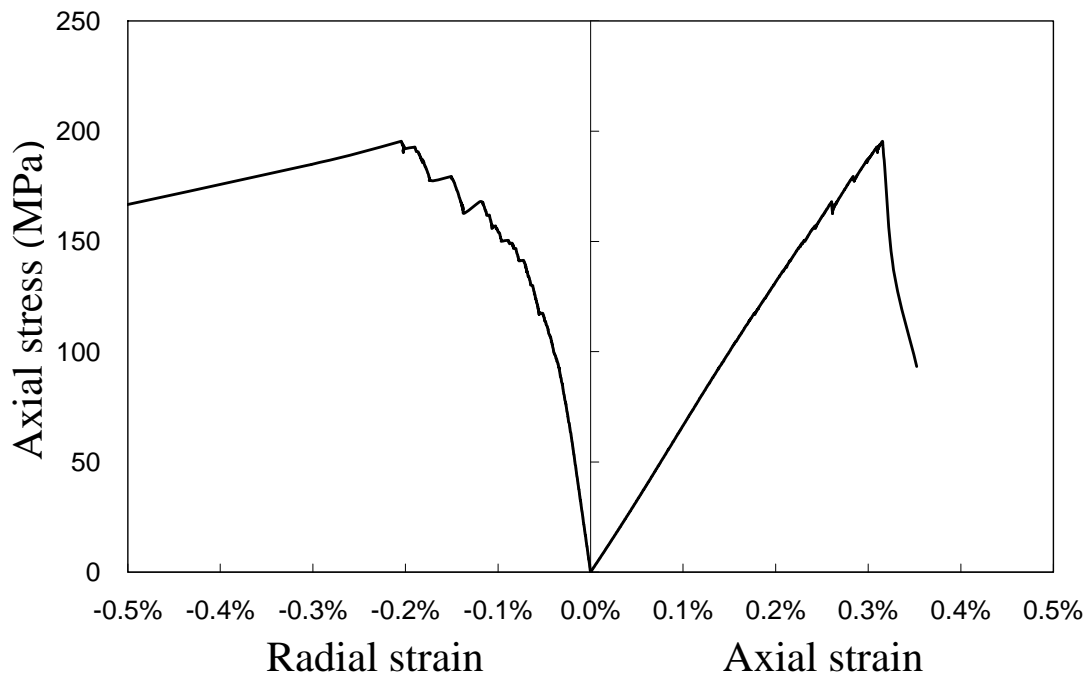
(c) Process (b) is repeated four times to enclose the model.



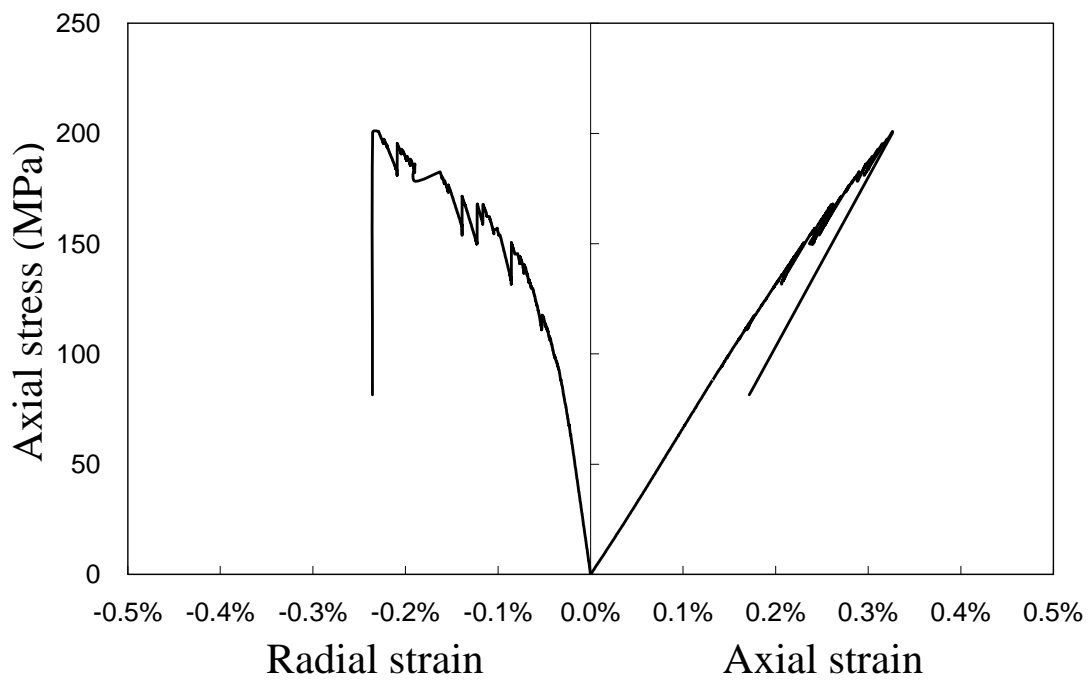
(d) Put on a new particle tangent to the pre-existing particles.

Fig.8 Particle packing method.





(a) Axial strain control.



(b) Radial strain control.

Fig.9 Complete stress-strain curves obtained from the simulation with different controlling methods.

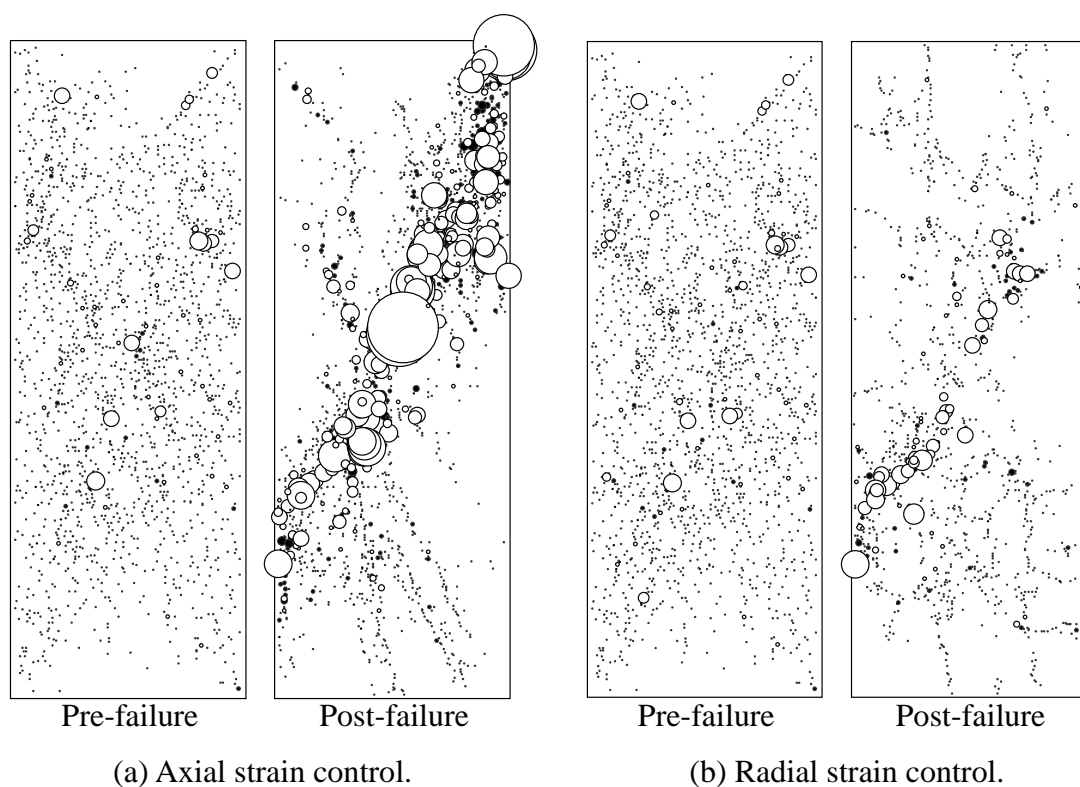
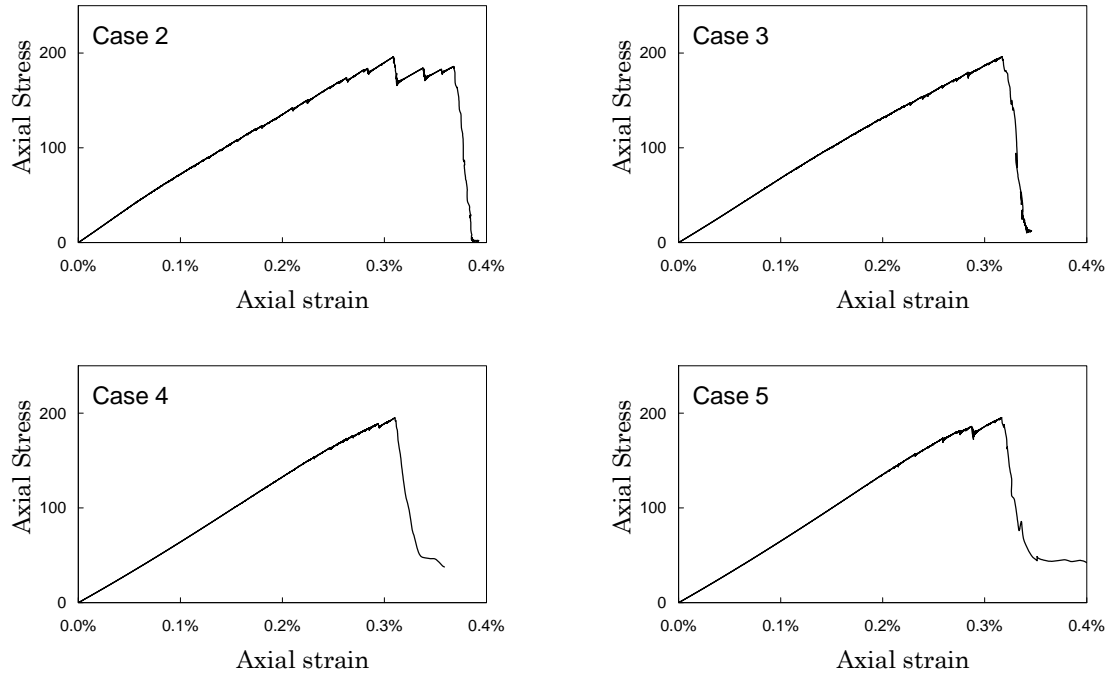
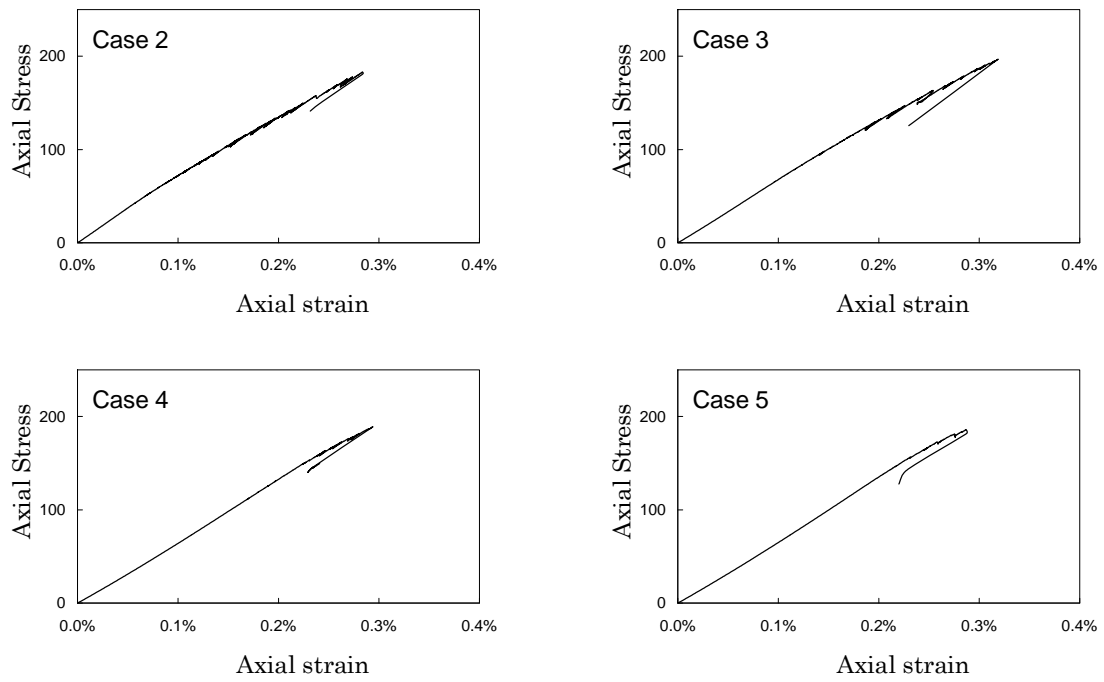


Fig.10 Spatial distribution of all the cracks for case1 in pre-failure region (left) and post-failure region (right). (a) axial strain control and (b) radial strain control. Tensile and shear cracks are expressed as filled and open circles, respectively. The diameters of each circle correspond to their respective magnitudes of energy.



(a) Axial strain control.



(b) Radial strain control.

Fig.11 Complete stress-strain curves obtained from each case.

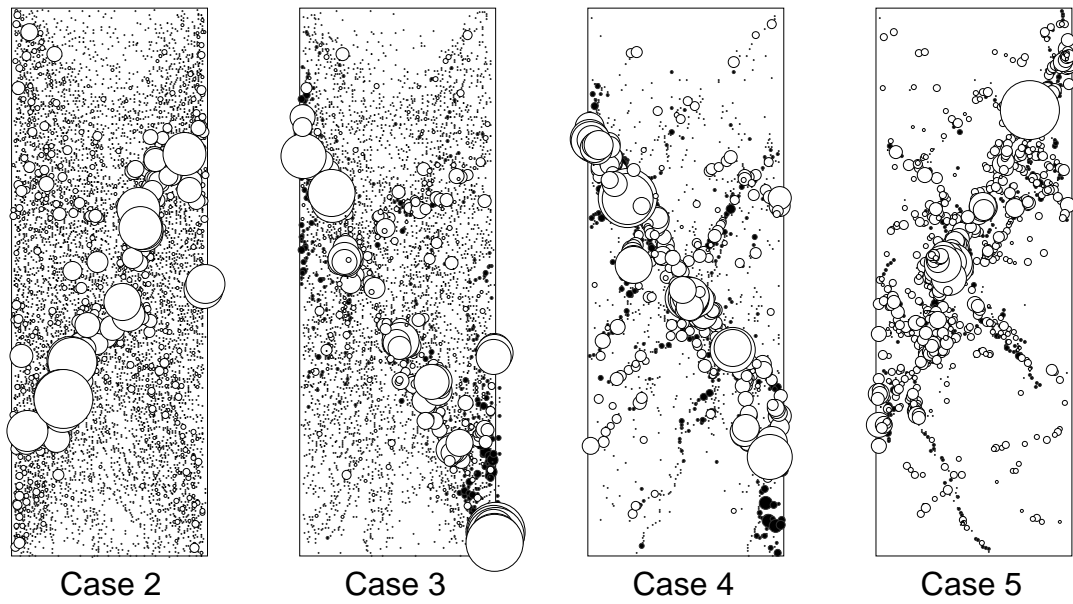


Fig.12 Spatial distribution of all the cracks for each cases. These figures are obtained from axial strain controlled uniaxial compression tests. Tensile and shear cracks are expressed as filled and open circles, respectively. The diameters of the circles correspond to their respective magnitudes of energy.

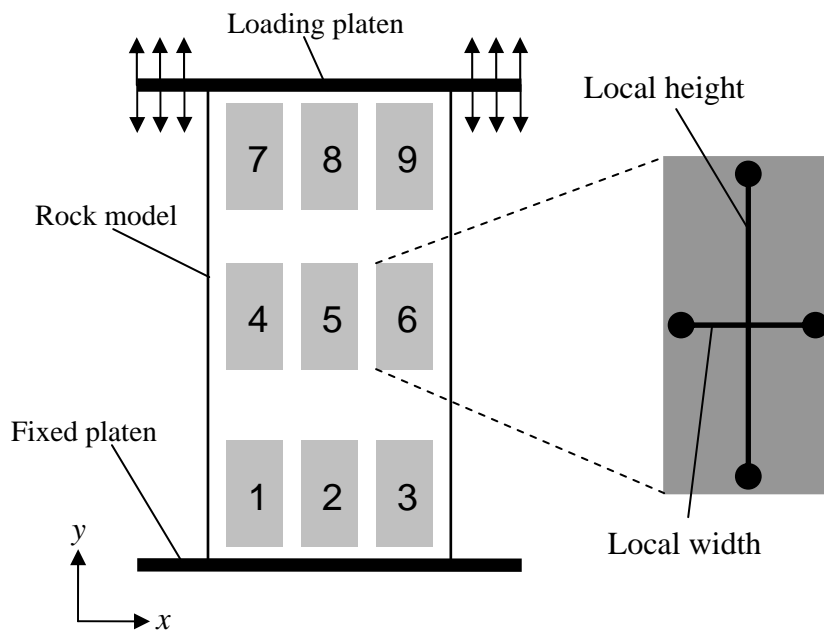
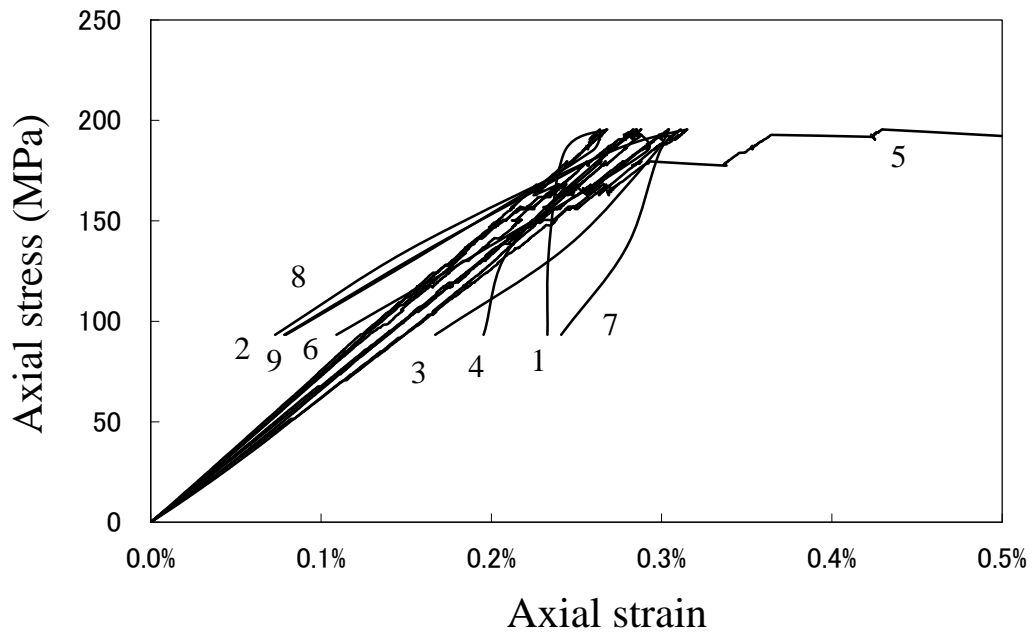
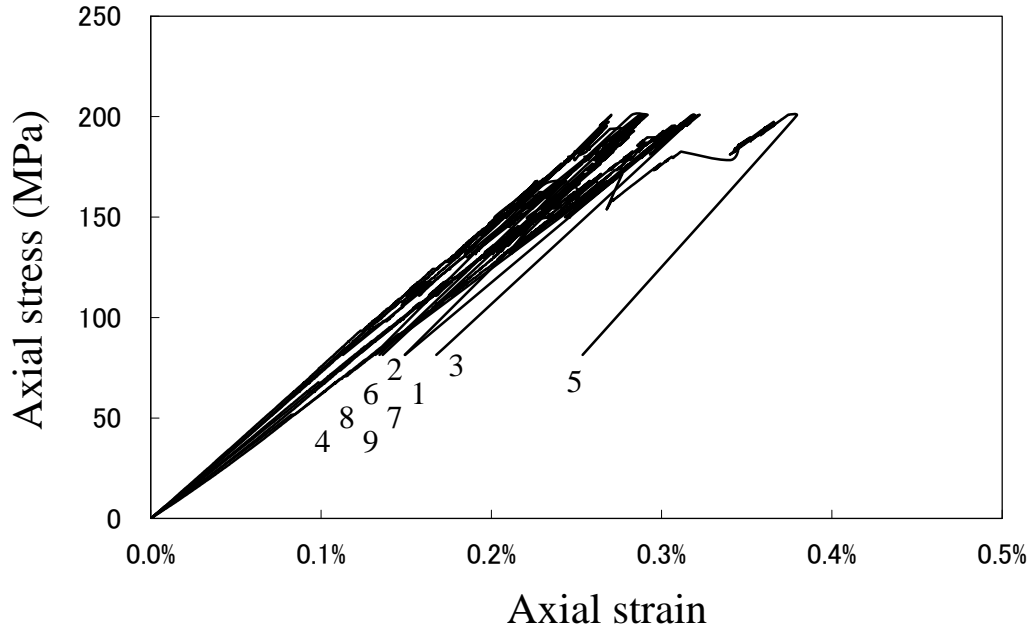


Fig.13 Local strain monitoring procedure in each region.



(a) Axial strain control.



(b) Radial strain control.

Fig.14 Local stress-strain curves in each region. The numbers in the figure represent the region number shown in Fig.13.